Acta Geochim (2017) 36(2):329–338
DOI 10.1007/s11631-017-0150-x

ORIGINAL ARTICLE

Zircon U–Pb dating and whole-rock elemental geochemistry of the Shazi anatase deposit in Qinglong, Western Guizhou, SW China

Jun Sun[1,2] · Zhao Jingyu[3] · Aiguo Nie[2]

Received: 23 November 2016 / Revised: 14 January 2017 / Accepted: 15 March 2017 / Published online: 23 May 2017
© Science Press, Institute of Geochemistry, CAS and Springer-Verlag Berlin Heidelberg 2017

Abstract The Shazi deposit is a large-scale anatase deposit in Qinglong, Guizhou Province. Zircon grains from this deposit yielded a zircon U–Pb age of ~259 Ma, representing the formation age of the deposit's parent rocks. This age is identical to the eruption age of the Emeishan large igneous province, indicating a synchronous magmatic event. The rare-earth-element patterns of laterite samples were similar to those of the weathered basalt sample, and sub-parallel to those of the Emeishan high-Ti basalts, implying a genetic relationship between the laterite and the basalt. The Chemical Index of Alteration values of laterite ranged from 96 to 98, suggesting a high degree of weathering. SiO_2, MgO, and alkaline metal elements decreased with increasing degree of weathering, while Al_2O_3, Fe_2O_3, and TiO_2 increased. We found the highest TiO_2 in laterite and the lowest in pillow basalts, indicating that Ti migrated from basalt to laterite. Our U–Pb dating and whole-rock elemental geochemistry analyses suggest that the Emeishan basalt is the parent rock of the Shazi anatase ore deposit. Based on our analysis, we propose a metallogenic model to explain the ore-forming process, in which the karst terrain formed by the Emeishan mantle plume and the subsequent basaltic magma eruption were the key factors in the formation the Shazi anatase ore deposit.

✉ Aiguo Nie
nieaiguo@163.com

[1] College of Resource and Environment Engineering, Guizhou University, Guizhou 550025, China

[2] College of Resource and Environment Engineering, Guizhou Institute of Technology, Guizhou 550003, China

[3] Key Laboratory of High-temperature and High-pressure Study of the Earth's Interior, Institute of Geochemistry, Chinese Academy of Sciences, Guizhou 550081, China

Keywords Anatase deposit · Zircon U–Pb · Emeishan basalt · Karst terrain

1 Introduction

Among the three naturally occurring polymorphs of TiO_2 (anatase, rutile, and brookite), rutile is the most stable and the most widely distributed, while anatase is the least stable. As an early metamorphic product of titaniferous rock, anatase commonly crystallizes under low-temperature and low-pressure conditions (Винчелл and Винчёел 1953; Doucet and Synthese 1967; Zhao et al. 2012). Anatase usually transforms into the relatively stable brookite and then into the most stable rutile through further metamorphism. Therefore, it is rare to find anatase as an independent titanium deposit in nature, and more common to see a paragenesis of rutile and brookite (Hebert and Gauthier 2007). Turner (1986) found a super-large-size anatase ore deposit in Tapira, Brazil, and proposed that it was formed by deep weathering of a perovskite- and pyroxene-rich alkaline pyroxenite. In China, before the discovery of the Shazi anatase ore deposit, the only confirmed independent titanium deposit was the Yangtizishan-Moshishan anatase ore deposit in Inner Mongolia (Zhao et al. 2006, 2008a, b).

The Shazi anatase was discovered in 2007 in Qinglong, Guizhou Province. As the first large-sized eluvial-type anatase ore deposit to be discovered in the Emeishan basalt weathering profile (Zhang et al. 2014a, b), it has great significance for the reevaluation, prospecting, and exploration of ore resources in Southwest Guizhou Province. A general survey and detailed geological exploration were carried out on this deposit from 2007 to 2011.

In this paper, we present zircon U–Pb dating and major- and trace-element geochemistry of both the anatase ore-bearing laterite and the Emeishan basalts from the Shazi anatase ore deposit. These results help constrain the deposits' geochemical characteristics, material source, and parent rock ages, thus providing important insights into the ore-forming process of the Shazi antase deposit.

2 Geological background

The Shazi anatase ore deposit is located in Qinglong County, southwestern Guizhou Province, and lies in the intersecting triangular region of the Yadu-Ziyun, Nayong-Wengan, and Nanpanjiang Faults (Fig. 1). Regionally, outcropping rocks include the Permian Maokou Formation, Emeishan volcanic successions, the Longtan Formation, and Quaternary sediments. The Maokou formation mainly consists of medium-bedded to massive biograin limestones and biograin micritic limestones. The Emeishan volcanic successions unconformably overlie the late Middle Permian Maokou Formation, and are unconformably overlain by the upper Permian Longtan Formation. The Emeishan volcanic successions are comprised of basaltic lava, volcanoclastic rock, basaltic tuff, and tholeiite. The Longtan Formation consists of sandstone, politic siltstone, and silty mudstone interbedded with bioclastic limestone.

Shazi anatase is found in Quaternary cliff debris and collapsed materials overlying a karst erosional surface of the Maokou Formation. The anatase ore-bearing layer is Quaternary Laterite. It contains three anatase orebodies: No. 1, No. 2, and No. 3 (Fig. 2).

Mine ores are commonly a mixture of clays, siliceous rocks, and limonite blocks, in which kaolinite, hydromica, montmorillonite, quartz, hydrogoethite, calcite, dolomite, jarosite, gypsum, pyrite, and arsenopyrite are prominent minerals.

3 Samples and analytical methods

Fourteen samples were taken from orebodies No. 2 and No. 3, from basalt between orebodies No. 1 and No. 2, and from the Maokou Formation. The basalt samples show pillow structures, indicative of a submarine environment, and contain variable proportions of clinopyroxene (10 vol%–15 vol%), plagioclase (5 vol%–15 vol%), and olivine (3 vol%–5 vol%) phenocrysts, set in a fine-grained to aphanitic groundmass composed of plagioclase, clinopyroxene, and minor apatite and opaque oxides.

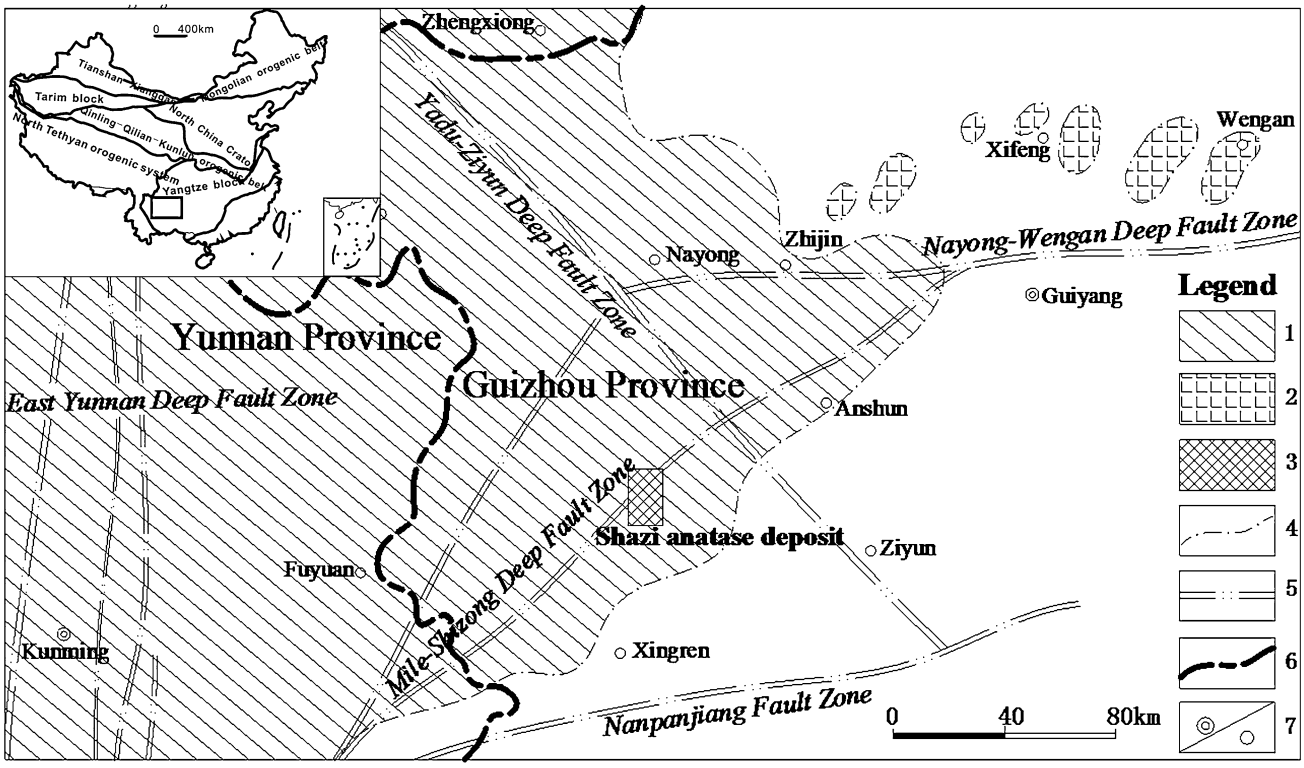

Fig. 1 Simplified geological map showing the location of the Shazi anatase deposit and the distribution of the Emeishan basalt in Guizhou. *1* Emeishan basalt widely distributed region, *2* Emeishan basalt scatteredly distributed region, *3* Shazi anatase ore zone in Qinglong County, *4* distribution boundary of the Emeishan basalt, *5* fault zone, *6* provincial boundary, *7* provincial capital/county. Data source: Gao and Li (2002); Guizhou Bureau of Geology and Mineral Resources (1987), etc.

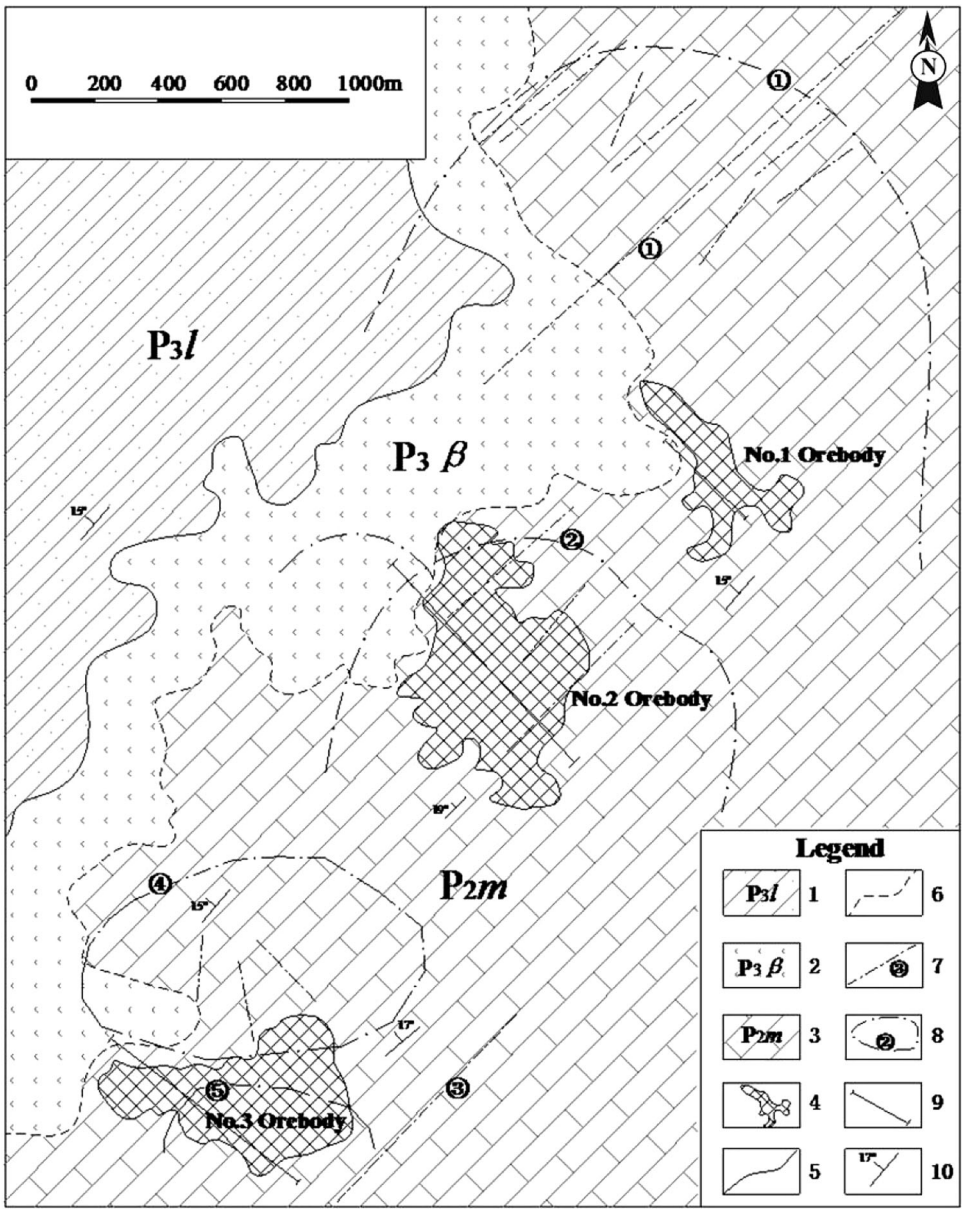

Fig. 2 Geological sketch map of the Shazi anatase ore deposit. *1* Upper Permian Longtan Formation coal series, *2* Emeishan basalt, *3* Middle Permian Maokou Formation limestone, *4* anatase orebody, *5* geological boundary, *6* karst uncomformable boundary, *7* linear structure explained on the basis of remote sensing, *8* circular structure explained on the basis of remote sensing, *9* representative prospecting line profile, *10* attitude of strata

Metamorphism of the basalt samples is represented by alteration of plagioclase to albite and some chloritization of groundmass and ferromagnesium mineral phases.

All samples were crushed and powdered with an agate mill to 200-mesh. Major element abundances in whole rocks were determined on fused glass discs using an AXIOS-PW4400 X-ray fluorescence (XRF) instrument in the State Key Laboratory of Ore Deposit Geochemistry (SKLODG), Institute of Geochemistry, Chinese Academy of Sciences. The accuracy was monitored using a Chinese national standard (GSR3). The standard deviations for the standard analyzed were generally better than 2%. The loss-on-ignition (LOI) was determined by the weight loss of a powered sample after 1 h at 1000 °C.

Trace element concentrations were analyzed using a Perkin-Elmer Sciex Elan DRC-e quadrupole inductively coupled plasma mass spectrometry (ICP-MS) in SKLODG. For each sample, 50 mg of powder was dissolved using a mixture of HF and HNO3 in a Teflon bomb for 48 h at 190 °C. Rhodium was used to monitor signal drift during data acquisition. The international standards GBPG-1 and OU-6, and the Chinese national standards GSR-1 and GSR-3, were used to monitor accuracy. The difference between our results and the recommended values for the standards was generally better than 10%.

Zircons from the Shazi anatase ore-bearing lateritic layer were separated by heavy liquid and magnetic separation methods. Pure zircons were handpicked under a

Table 1 LA-ICP-MS zircon U–Pb analytical results of the Shazi anatase deposit

No.	Pb (ppm)	Th (ppm)	U (ppm)	$^{207}Pb/^{206}Pb$		$^{207}Pb/^{235}U$		$^{206}Pb/^{238}U$		$^{207}Pb/^{206}Pb$		$^{207}Pb/^{235}U$		$^{206}Pb/^{238}U$	
				Ratio	1σ	Ratio	1σ	Ratio	1σ	Age (Ma)	1σ	Age (Ma)	1σ	Age (Ma)	1σ
SZ16-01	10.70	142.79	158.33	0.0942	0.0030	0.5381	0.0164	0.0415	0.0005	1522.2	60.3	437.1	10.9	262.2	3.4
SZ16-02	10.72	143.19	157.00	0.0941	0.0030	0.5404	0.0166	0.0418	0.0005	1510.8	60.0	438.7	11.0	263.7	3.3
SZ16-03	10.13	130.84	174.35	0.0754	0.0022	0.4248	0.0127	0.0409	0.0006	1079.6	59.3	359.5	9.1	258.2	3.5
SZ16-04	10.36	134.81	173.57	0.0816	0.0040	0.4593	0.0252	0.0408	0.0009	1235.2	96.6	383.8	17.5	258.1	5.7
SZ16-05	7.32	92.58	126.72	0.0608	0.0019	0.3433	0.0109	0.0411	0.0006	631.5	66.7	299.6	8.3	259.6	3.6
SZ16-06	7.33	92.45	126.53	0.0607	0.0019	0.3417	0.0108	0.0409	0.0006	627.8	66.7	298.5	8.2	258.7	3.6
SZ16-07	7.45	94.46	128.12	0.0605	0.0019	0.3398	0.0111	0.0408	0.0006	620.4	68.5	297.0	8.4	258.1	3.7
SZ16-08	7.59	96.39	129.53	0.0606	0.0020	0.3397	0.0115	0.0408	0.0006	633.4	70.4	296.9	8.7	257.8	3.8
SZ16-09	7.77	98.70	131.79	0.0597	0.0021	0.3345	0.0118	0.0407	0.0006	594.5	108.3	293.0	9.0	257.5	3.9
SZ16-10	10.34	135.06	143.43	0.0904	0.0030	0.5196	0.0165	0.0420	0.0007	1435.2	61.9	424.9	11.0	265.5	4.2
SZ16-11	10.28	132.96	144.29	0.0911	0.0027	0.5175	0.0150	0.0416	0.0006	1450.0	57.4	423.5	10.1	262.6	3.8
SZ16-12	10.07	133.97	161.82	0.0771	0.0021	0.4365	0.0116	0.0410	0.0005	1124.1	53.2	367.8	8.2	259.2	3.2
SZ16-13	6.73	70.56	97.20	0.1016	0.0038	0.5634	0.0169	0.0417	0.0008	1653.7	68.7	453.8	11.0	263.3	4.8
SZ16-14	11.33	110.57	134.50	0.0810	0.0042	0.4529	0.0258	0.0407	0.0010	1220.4	101.9	379.3	18.0	257.1	6.0
SZ16-15	6.32	94.46	110.23	0.0624	0.0020	0.3466	0.0109	0.0406	0.0006	687.1	68.5	302.2	8.2	256.6	3.6
SZ16-16	6.24	94.79	109.58	0.0621	0.0020	0.3417	0.0110	0.0402	0.0006	675.9	70.4	298.5	8.3	254.0	3.6
SZ16-17	6.24	95.37	109.01	0.0615	0.0019	0.3444	0.0111	0.0407	0.0006	657.4	68.5	300.5	8.4	257.4	3.7
SZ16-18	6.17	95.08	107.96	0.0631	0.0020	0.3515	0.0110	0.0407	0.0006	710.8	66.7	305.9	8.3	257.1	3.6
SZ16-19	6.11	95.27	107.26	0.0632	0.0020	0.3510	0.0111	0.0406	0.0006	722.2	70.4	305.5	8.3	256.4	3.7

binocular microscope, then mounted in epoxy resin and polished until the grain interiors were exposed. Cathodoluminescence (CL) images were obtained using a JSM6510 scanning electron microscope, manufactured by the JEOL Corporation (Japan), at the Beijing zircon dating navigation technology limited company.

The U–Pb dating of zircon was also conducted by LA-ICP-MS at SKLODG. A GeoLasPro laser-ablation system (Lamda Physik, Gottingen, Germany) and Agilent 7700x ICP-MS (Agilent Technologies, Tokyo, Japan) were used to determine ages. The 193 nm ArF excimer laser, homogenized by a set of beam delivery systems, was focused on the zircon surface with a flux of 10 J/cm^2. Ablation protocol employed a spot diameter of 32 μm at 5 Hz repetition rate for 40 s (equating to 200 pulses). Helium was applied as a carrier gas to efficiently transport aerosol to ICP-MS. Zircon 91500 was used as an external standard to correct instrumental mass discrimination and elemental fractionation. Zircon GJ-1 and Plešovice were used as quality control for geochronology. Common lead concentration of zircon was externally calibrated against NIST SRM 610 using Si as the internal standard, while Zr

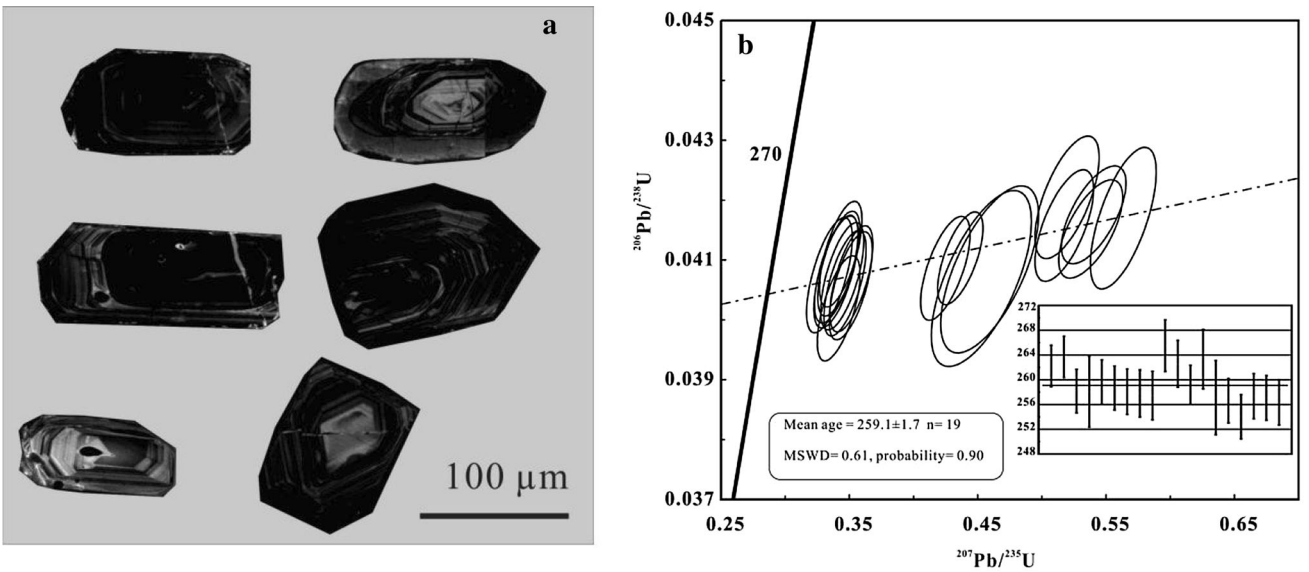

Fig. 3 **a** cathodoluminescence (CL) images of representative zircons and **b** LA-ICP-MS U–Pb Concordant diagrams for zircons from the Shazi anatase deposit

was used as the internal standard for other trace elements (Liu et al. 2010c; Hu et al. 2011).

Raw data reduction was performed off-line by ICPMS-DataCal (Liu et al. 2010b, c). As $^{207}Pb/^{206}Pb$ ages are sensitive to the common lead correction, the $^{206}Pb/^{238}U$ age is normally adopted for samples (Claoué-Long et al. 1991).

4 Results

4.1 Zircon U–Pb age

The measured U–Pb isotope compositions of zircon grains from the Shazi deposit are listed in Table 1. CL images of zircons are shown in Fig. 3a. The zircons were subhedral, transparent to light brown, and prismatic in shape with length to width ratios of 1:1 to 2:1; they exhibited a similar internal morphology with magmatic oscillatory zoning. Nineteen analyses on separate grains showed a range of Th (70–143 ppm) and U (97–170 ppm) contents with relatively high Th/U ratios (0.73–0.94), indicative of a magmatic origin. These analyses yielded a weighted mean $^{206}Pb/^{238}U$ of 259.1 ± 1.7 with a MSWD value of 0.61 (Fig. 3b). We consider this age to represent the crystallization age of these magmatic zircons.

4.2 Major and rare earth elements

Major oxide compositions of the investigated rock samples are shown in Table 2. One sample (T-005) was basaltic andesite and had a relatively high SiO_2 content (57.37 wt%). The pillow basalt was analyzed as 47.51 wt%–49.70 wt% SiO_2, 2.91 wt%–3.60 wt% TiO_2, 13.74 wt%–20.75 wt% TFe_2O_3, 14.62 wt%–14.98 wt% Al_2O_3, and 3.40 wt%–6.42 wt% $Na_2O + K_2O$. The weathered basalt was distinguished from the fresh basalt samples by higher TiO_2 (3.00 wt%–3.51 wt%) and Al_2O_3 (18.53 wt%–26.11 wt%), and lower SiO_2 (38.50 wt%–47.89 wt%) and $Na_2O + K_2O$ (1.87 wt%–2.87 wt%). The laterites had the highest contents of TiO_2 (4.80 wt%–5.37 wt%) and TFe_2O_3 (23.53 wt%–28.95 wt%), and lowest contents of SiO_2 (31.04 wt%–33.69 wt%) and alkaline metal ($CaO + Na_2O + K_2O < 1$ wt%). Limestone samples from the Maokou formation were dominated by $CaCO_3$ with ~55 wt% CaO.

Trace element compositions of the investigated rock samples are shown in Table 2. The rare earth element (REE) contents of the ore-bearing laterite, weathered basalts, pillow basalts, and limestone ranged from 250 to 300, 270 to 365, 138 to 173, and 3.5 to 16.6 ppm, respectively. The chondrite-normalized REE patterns of all samples except for limestone showed LREE enrichment, and were similar to those of the Emeishan high-Ti lavas (Xiao et al. 2004; Xu et al. 2001) (Fig. 4).

5 Discussion

5.1 Relationship between laterite and Emeishan basalt

The Emeishan basalt large igneous rock province lies in the Sichuan–Yunnan–Guizhou region of southern China. It was formed by enormous quantities of mafic volcanic successions, numerous contemporaneous mafic intrusions,

Table 2 Major oxides (wt%) and trace elements (ppm) compositions of fourteen samples from the Shazi anatase deposit in Western Guizhou

Rock types	Laterite				Weathered basalt		Pillow-basalt				Basaltic andesite	Limestone		
Sample No.	2-011	2-012	3-003	3-004	2-002	2-004	T-002	T-003	T-004	T-007	T-005	2-008	3-001	3-002
SiO_2	31.72	31.88	33.69	31.04	38.50	47.89	47.69	47.51	49.70	48.52	57.37	2.09	0.35	0.28
TiO_2	4.80	4.78	5.37	5.08	3.51	3.00	3.26	3.24	3.60	2.91	2.63	0.07	0.04	0.02
Al_2O_3	21.91	21.88	18.41	23.69	26.11	18.53	14.98	14.66	14.62	14.82	12.21	0.43	0.16	0.06
TFe_2O_3	23.53	23.59	28.95	24.46	15.12	14.60	15.51	15.41	20.75	13.74	17.18	0.25	0.20	0.07
MgO	0.23	0.24	0.42	1.20	0.50	0.37	4.99	5.00	2.10	3.13	0.78	0.17	0.56	0.49
CaO	0.29	0.13	0.37	0.12	1.16	1.57	6.12	6.12	0.47	4.08	1.68	54.50	55.50	55.70
MnO	0.21	0.21	0.29	0.30	0.12	0.12	0.24	0.22	0.14	0.19	0.05	0.07	0.01	0.01
Na_2O	0.04	0.04	0.02	0.03	0.06	0.08	2.99	2.83	4.81	6.42	6.60	0.01	0.01	0.01
K_2O	0.31	0.31	0.03	0.20	1.81	2.79	0.66	0.57	0.01	0.01	0.02	0.08	0.01	0.01
P_2O_5	0.32	0.32	0.48	0.34	0.22	0.35	0.35	0.35	0.12	0.33	0.36	0.01	0.01	0.01
LOI	15.72	15.32	11.04	13.07	12.14	8.30	2.95	2.90	3.53	4.87	1.41	42.74	43.18	43.53
Total	99.08	98.70	99.07	99.53	99.25	97.60	99.74	98.81	99.85	99.02	100.29	100.42	100.03	100.19
CIA	95.93	97.17	96.15	98.00	86.24	75.52	47.19	47.20	62.48	45.17	46.70	0.43	0.16	0.06
Sc	48.6	48.7	54.6	46.3	35.2	29.6	30.6	31.4	31.4	27.5	21.1	5.1	0.9	0.6
La	46.5	48.4	23.4	59.8	51.3	81.9	27.6	29.2	24.2	31.3	22.6	2.7	1.3	0.9
Ce	121.5	124.0	87.0	93.0	90.2	138.0	61.4	66.1	56.6	68.3	52.0	4.8	2.1	1.3
Pr	13.0	13.3	4.9	14.7	10.9	18.2	7.4	7.8	5.8	7.5	6.4	0.5	0.2	0.1
Nd	53.7	56.5	18.3	58.2	45.5	69.7	29.6	32.3	23.1	30.7	26.4	2.1	0.7	0.5
Sm	12.2	13.2	4.8	12.7	10.8	14.6	7.3	7.6	5.2	7.2	6.7	0.7	0.2	0.1
Eu	3.9	4.1	1.8	4.0	3.5	3.8	2.6	2.7	2.1	2.4	2.4	0.3	0.1	0.0
Gd	11.6	12.4	5.1	13.2	14.8	11.6	7.9	8.2	5.6	7.1	7.2	1.6	0.2	0.1
Tb	1.8	1.8	0.9	2.0	2.6	1.8	1.3	1.3	0.9	1.1	1.1	0.3	0.0	0.0
Dy	10.7	10.9	6.9	12.3	16.8	10.7	8.0	7.8	5.9	7.2	6.8	1.8	0.2	0.1
Ho	2.1	2.3	1.7	2.5	3.7	2.2	1.7	1.6	1.3	1.5	1.3	0.4	0.0	0.0
Er	5.7	6.1	5.4	6.9	9.9	6.2	4.6	4.3	3.5	4.1	3.6	0.7	0.1	0.1
Tm	0.8	0.8	0.9	0.9	1.3	0.9	0.6	0.6	0.5	0.5	0.5	0.1	0.0	0.0
Yb	4.7	5.1	5.6	5.3	7.7	5.2	3.6	3.4	3.0	3.3	2.8	0.5	0.1	0.1
Lu	0.7	0.7	0.9	0.8	1.1	0.8	0.5	0.5	0.4	0.5	0.4	0.1	0.0	0.0
ΣREE	288.5	299.6	167.5	286.2	269.9	365.5	164.0	173.3	138.1	172.7	140.0	16.6	5.3	3.5
LREE	250.7	259.5	140.1	242.4	212.1	326.2	135.9	145.8	117.0	147.4	116.4	11.2	4.5	3.0
HREE	37.8	40.1	27.4	43.8	57.8	39.3	28.2	27.6	21.1	25.3	23.6	5.4	0.8	0.5
δCe	1.19	1.18	1.90	0.75	0.89	0.84	1.03	1.05	1.13	1.06	1.05	0.93	0.92	0.80
δEu	0.98	0.96	1.08	0.94	0.84	0.86	1.05	1.05	1.17	1.03	1.03	0.92	0.82	0.80
(La/Sm)N	2.47	2.37	3.17	3.05	3.07	3.62	2.44	2.47	3.00	2.83	2.18	2.42	4.66	6.00

and minor felsic magma eruption (Chung and Jahn 1995) in the mid- to late Permian. Eruption of the Emeishan basalt is commonly regarded as the result of mantle plume uplift (Xu et al. 2001; Zhou et al. 2002; Sun et al. 2010). The ages of Emeishan flood basalts were originally inferred from the U–Pb ages of zircon from coeval mafic–ultramafic intrusions in the region (~260 Ma) (Guo et al. 2004; He et al. 2007) and from $^{40}Ar/^{39}Ar$ dating results on the Emeishan basalts (Boven et al. 2002). In the present study, zircon grains from the Shazi large-size anatase deposit yielded a weighted mean age of ~259 Ma, representing the formation age of the parent rocks. The two ages are identical within the stated error, indicating a synchronous magmatic event. The similarity of REE patterns between the laterite and basalt confirms the genetic relationship between them.

Emeishan basalts have been proven as the material source of many supergene weathering or sedimentary ores.

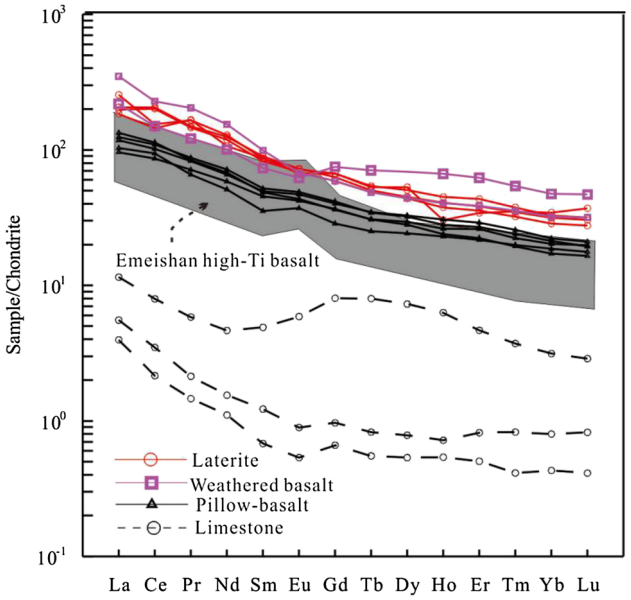

Fig. 4 Chondrite-normalized REE patterns for laterite, weathered basalt, basalt, and limestone of the Shazi anatase deposit. Data of chondrite are from Sun and McDonough (1989)

Previous studies proved that the Emeishan basalt provided source material for the supergene minerals (e.g. bauxite ores in Quyang, Pingguo, and Jinxi in West Guangxi) through weathering and denuding processes (Deng et al. 2010; Liu et al. 2010a; Wang et al. 2010). Sedimentary environment research on the Xuanwei formation by Sr isotope analysis assumed that Sr of the REE-enriched shale strata might have come from the Emeishen basalt (Zhang et al. 2010). Zhou et al. (2013) further substantiated the interrelationship between the paleo-weathering sedimentary-type crust REE deposits and the weathering of the Emeishan basalt.

Major elements usually indicate the weathering degree of the parent rocks. The Chemical Index of Alteration ($CIA = [(Al_2O_3)/(Al_2O_3 + CaO + Na_2O + K_2O)] \times 100$) pioneered by Nesbitt and Young (1982), with values expressed as molar proportions, is used to reflect leaching of base components compared with Al during surface weathering (McLennan 1993). If all the rocks are feldspars, then the CIA will be 50; if biotites, hornblendes or pyroxenes, the CIA will be 50–55, 10–30, or 0–10; for secondary clay minerals like kaolinites and gibbsites, the CIA is 100; for illites and smectite, the CIA is 75–85 (Nesbitt and Markovics 1997). Thus, a higher CIA indicates a deeper degree of weathering. As shown by Fig. 5, laterite samples had the highest CIA, while the pillow basalts had lower ones, and limestone the lowest because it was not exposed to the surface. With increasing degree of weathering, SiO_2, MgO, and alkaline metal elements decreased, while Al_2O_3, Fe_2O_3, and TiO_2 increased. Increased Al_2O_3 is also attributable to the formation of clay minerals, such as kaolin. Increased TiO_2 indicated an enrichment of anatase during weathering; the highest TiO_2 being found in laterite and the lowest in pillow basalts suggests that Ti migrated from basalt to laterite.

5.2 Ore-forming elements of Ti and Sc

TiO_2 contents in laterites ranged from 4.80 wt% to 5.37 wt%, with an average value of 5.0 wt%—around 1.7 times that of the upper continental crust. Although TiO_2 is generally considered stable, Ti has been found to be mobile in extreme chemical weathering processes in tropical areas (Braun et al. 1993; Walter et al. 1995; Patino et al. 2003), and organic complexation of Ti can significantly enhance its mobility (Ma et al. 2007; Viers et al. 1997). It has been inferred that the western Guizhou area was quite heavily exposed to late-Permian weathering, leading to the leaching loss of the relatively stable TiO_2 (Zhou et al. 2013). Taken together, this evidence suggests that the Shazi anatase ore deposit escaped strong weathering and was well-preserved by the overlying Emeishan basalt and Longtan coal-bearing sedimentary formation.

Scandium was conspicuously enriched in the ore samples of the three orebodies with contents ranging from 46.3 to 54.6 ppm, and an average value of 49.6 ppm—4.5 times that of the upper continental crust (Table 2). In nature, Sc is stable in the form of Sc^{3+} (Liu et al. 1984), which is present in pyroxene, hornblende, and olivine through replacement of Fe^{2+} and Mg^{2+} (Lü et al. 1992). In the Shazi anatase ore deposit, Sc^{3+} is mainly found in pyroxenes in basalts and coexists isomorphically with Fe, Mn, and Ti. When the Emeishan basalt erupted, huge quantities of eruptive materials were exposed and dropped into the brine of the karst depression; Sc^{3+} would have bene released from pyroxene by weathering and disintegration. As a consequence, $Sc(OH)_3$ or Sc_2O_3 formed and then was adsorbed on colloidal clay minerals, resulting in the enrichment of Sc in the anatase orebody.

5.3 Ore forming process

Based on zircon U–Pb dating and geochemical analyses of laterite and Emeishan basalt samples, the deduced ore-forming process of the Shazi large anatase deposit can be divided into six stages as follows:

Stage 1 The crust was rapidly uplifted by the mantle plume, and the Maokou formation limestone outcropped on the surface and formed a karst terrain.

Stage 2 The Tethys Sea's transgression formed large quantities of paleo-geomorphological karst highlands

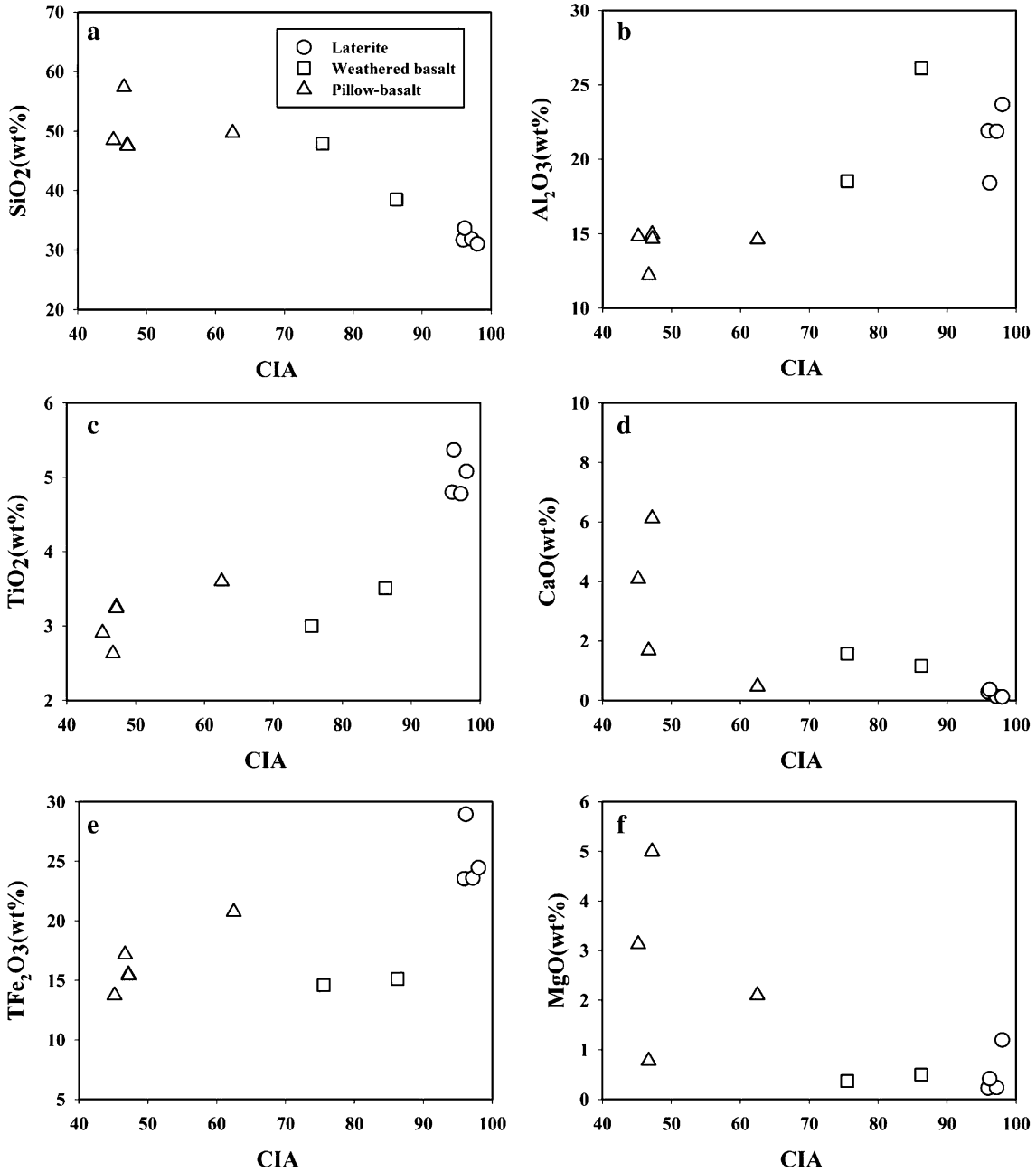

Fig. 5 Plots of the Chemical alternation index (CIA) versus major elements for laterite, weathered basalt, and fresh basalt samples from the Shazi large-size anatase deposit

and karst depressions at the top of the Middle Permian Maokou Formation limestone around the Shazi region. Near-shore tidal flats brought brine into the karst depressions (Wang 1994).

Stage 3 At the late Maokou stage of the Middle Permian, the Emeishan basalt erupted. Huge quantities of mafic basalt, mafic lava, and intermediate acid felsic intrusion rocks were exposed and fell into the brine of the karst depression, forming a hydrothermal system with low temperature, low pressure, and weak alkaline conditions. Based on the thickness of pyroclastic sediments, the depth of the hydrothermal water was deduced to be several tens of meters, creating a certain static pressure.

Stage 4 In the hydrothermal system described above, the Emeishan basalt materials eroded and disintegrated and water–rock reactions occurred. The Emeishan Basalts

from the Shazi region are enriched in Na but depleted in K; Ti mostly entered the silicon–oxygen tetrahedral of pyroxene by heterovalent isomorphism. Hydrolysis released Ti and Sc from minerals such as pyroxene and plagioclase. The Na-rich feldspars eroded and decomposed. Na^+ was dissolved in brine, while K^+ migrated into clay minerals. The karst-depression water body was initially separated and isolated by karst highland, and then a special geochemical barrier with weakly alkaline brine formed in the ground oxidation zone of the karst depression, providing sufficient oxygen for TiO_2 formation. This special geochemical barrier also provided the necessary environmental conditions for anatase crystallization.

Stage 5 During the Longtan stage of the Early Permian, a paralic epicontinental sea deposit—the Longtan—formed over the Emeishan basalt, preserving the underlying anatase. Neither the sedimentation since the Late Permian nor the tectonism of the Yanshanian generated sufficiently high temperature and pressure to convert the anatase into rutile. Therefore, the anatase orebody was preserved stably during this stage.

Stage 6 Hercynian and neotectonic movements exposed the anatase orebody on the ground surface. After Quaternary weathering and decomposition, the carbonate rocks such as anatase-enriched basalts further weathered and decomposed to soil. The soil layers were then further enriched in anatase and formed the residual deluvial-type anatase ore deposit, i.e. the Shazi anatase ore deposit.

6 Conclusion

1. Zircon grains from the Shazi large-size anatase deposit yielded a zircon U–Pb age of ~259 Ma, representing the formation age of the parent rocks. This age is identical to that for the mafic–ultramafic intrusions associated with the Emeishan LIP within the stated error, indicating a synchronous magmatic event.
2. The REE patterns of the laterite samples were similar to those of the basalt samples, implying a genetic relationship between the two.
3. The karst terrain formed by the Emeishan mantle plume, and the subsequent basaltic magma eruption, were key factors in the formation the Shazi anatase ore deposit.

Acknowledgements We thank the editors and the reviewers very much for their constructive comments that have greatly improved this manuscript. This study was supported by the Natural Science Foundation of China (Grant No. 41262005).

References

Boven A, Pasteels P, Punzalan LE, Liu J (2002) $^{40}Ar/^{39}Ar$ geochronological constraints on the age evolution of the Permo-Triaasic Emeishan Volcanic Province, Southwest China. J Asian Earth Sci 20(2):157–175

Braun JJ, Pagel M, Herbilln A, Rosin C (1993) Mobilization and redistribution of REEs and thorium in a syenitic lateritic profile: a mass balance study. Geochim Cosmochim Acta 57(18):4419–4434

Винчелл А, Винчёел Г (1953) Оптическая минералогия Изд .Иностранной Литературы (**in Russian**), Москва, Стр

Chung SL, Jahn B (1995) Plume–lithosphere interaction in generation of the Emeishan flood basalts at the Permian–Triassic boundary. Geology 23(10):889

Claoué-Long JC, Zhang Z, Ma G, Du S (1991) The age of the Permian–Triassic boundary. Earth Planet Sci Lett 105(1):182–190

Deng J, Wang Q, Yang S, Liu X, Zhang Q, Yang L, Yang Y (2010) Genetic relationship between the Emeishan plume and the bauxite deposits in Western Guangxi, China: constraints from U–Pb and Lu–Hf isotopes of the detrital zircons in bauxite ores. J Asian Earth Sci 37(5–6):412–424

Doucet S, Synthese DL (1967) Synthesis of wolframite, Cassiterite, and anatase at low temperature. Bulletin de la societe Francaise de Mineralogie et de Cristallographie 90(1):111–112

Gao ZM, Li HY (2002) Metallogenesis and prospecting of the main types of gold deposits in the Yunnan-Guizhou area. Geological Publishing House, Beijing (**in Chinese**)

Guizhou Bureau of Geology and Mineral Resources (1987) Regional geology of Guizhou Province. Geological Publishing House, Beijing (**in Chinese**)

Guo F, Fan W, Wang Y, Li C (2004) When did the Emeishan mantle plume activity start? Geochronological and geochemical evidence from ultramafic-mafic dikes in Southwestern China. Int Geol Rev 46(3):226–234

He B, Xu Y-G, Huang X-L, Luo Z-Y, Shi Y-R, Yang Q-J, Yu S-Y (2007) Age and duration of the Emeishan flood volcanism, SW China: geochemistry and SHRIMP zircon U–Pb dating of silicic ignimbrites, post-volcanic Xuanwei Formation and clay tuff at the Chaotian section. Earth Planet Sci Lett 255(3–4):306–323

Hebert E, Gauthier M (2007) Uncoventional rutile deposits in the Quebec Appalachians: product of hypogene enrichment during low-grade metamorphism. Econ Geol 102(2):319–326

Hu Z, Liu Y, Chen L, Zhou L, Li M, Zong K, Zhu L, Gao S (2011) Contrasting matrix induced elemental fractionation in NIST SRM and rock glasses during laser ablation ICP-MS analysis at high spatial resolution. J Anal At Spectrom 26(2):425–430

Liu Y, Cao L, Li Z (1984) Element geochemistry. Science Publishing House, Beijing **(in Chinese)**

Liu X, Wang Q, Deng J, Zhang Q, Sun S, Meng J (2010a) Mineralogical and geochemical investigations of the Dajia Salento-type bauxite deposits, western Guangxi, China. J Geochem Explor 105(3):137–152

Liu YS, Gao S, Hu ZC, Gao CG, Zong KQ, Wang DB (2010b) Continental and oceanic crust recycling-induced melt–peridotite interactions in the Trans-North China Orogen: U–Pb dating, Hf isotopes and trace elements in zircons from mantle xenoliths. J Petrol 51(1–2):537–571

Liu YS, Hu ZC, Zong KQ, Gao CG, Gao S, Xu J, Chen HH (2010c) Reappraisement and refinement of zircon U–Pb isotope and trace element analyses by LA-ICP-MS. Chin Sci Bull 55:1535–1546 **(in Chinese with English abstract)**

Lü X, Cheng X, Zhou G (1992) Occurrence state of scandium in PanZhiHua iron ore. Min Metall Eng 12(4):35–39 **(in Chinese)**

Ma JL, Wei GJ, Xu YG, Long WG, Sun WD (2007) Mobilization and re-distribution of major and trace elements during extreme weathering of basalt in Hainan Island, South China. Geochimica et Cosmochimica Acta 71(13):3223–3237

McLennan SM (1993) Weathering and global denudation. J Geol 101:295–303

Nesbitt HW, Markovics G (1997) Weathering of granodioritic crust, long-term storage of elements in weathering profiles, and petrogenesis of siliciclastic sediments. Geochim Cosmochim Acta 61(8):1653–1670

Nesbitt HW, Young G (1982) Early Proterozoic climates and plate motions inferred from major element chemistry of lutites. Nature 299(5885):715–717

Patino LC, Velbel MA, Price JR, Wade JA (2003) Trace element mobility during spheroidal weathering of basalts and andesites in Hawaii and Guatemala. Chem Geol 202(3–4):343–364

Sun SS, McDonough WF (1989) Chemical and isotopic systematics of oceanic basalts: implications for mantle composition and processes. In: Saunders AD, Norry MJ (eds) Magmatism in the ocean basins, vol 42. Geological Society, London, pp 313–345

Sun Y, Lai X, Wignall PB, Widdowson M, Ali JR, Jiang H, Wang W, Yan C, Bond DPG, Védrine S (2010) Dating the onset and nature of the Middle Permian Emeishan large igneous province eruptions in SW China using conodont biostratigraphy and its bearing on mantle plume uplift models. Lithos 119(1–2):20–33

Turner R (1986) Brazilian titanium. Eng Min J 187:40–42

Viers J, Dupré B, Polvé M, Schott J, Dandurand J-L, Braun J-J (1997) Chemical weathering in the drainage basin of a tropical watershed (Nsimi-Zoetele site, Cameroon): comparison between organic-poor and organic-rich waters. Chem Geol 140(3–4):181–206

Walter AV, Nahon D, Flicoteaux R, Girard JP, Melfi A (1995) Behaviour of major and trace elements and fractionation of REE under tropical weathering of a typical apatite-rich carbonatite from Brazil. Earth Planet Sci Lett 136(3–4):591–602

Wang L (1994) Permian paleogeography and metallogenesis in Southern China, vol Geological. Publishing House, Beijing **(in Chinese)**

Wang Q, Deng J, Liu X, Zhang Q, Sun S, Jiang C, Zhou F (2010) Discovery of the REE minerals and its geological significance in the Quyang bauxite deposit, West Guangxi, China. J Asian Earth Sci 39(6):701–712

Xiao L, Xu YG, Mei HJ, Zheng YF, He B, Pirajno F (2004) Distinct mantle sources of low-Ti and high-Ti basalts from the western Emeishan large igneous province, SW China: implications for plume–lithosphere interaction. Earth Planet Sci Lett 228:525–546

Xu Y, Chung SL, Jahn B, Wu G (2001) Petrologic and geochemical constraints on the petrogenesis of Permian–Triassic Emeishan flood basalts in southwestern China. Lithos 58(3–4):145–168

Zhang ZW, Yang XY, Li S, Zhang ZS (2010) Geochemical characteristics of the Xuanwei Formation in West Guizhou: significance of sedimentary environment and mineralization. Chin J Geochem 29(4):355–364

Zhang M, Nie A, Xie F, Zhang Z (2014a) Study on the geological conditions of metallogenesis of the Shazi large-scale anatase deposit in Qinglong County, Guizhou Province. Chin J Geochem 33(4):450–458

Zhang M, Nie A, Xie F, Zhu M, Zhang Z (2014b) Study on the element geochemical charactersitics of the Shazi large-sized anatase ore deposit in Qinglong, Guizhou Province. Chin J Geochem 33(3):316–323

Zhao Y, Li D, Chen W, Feng C, Sun W (2006) The Yangtizishan sedimentary-metamorphic-type Ti deposit in Inner Mongolia—discovery of a new type of Ti deposits. Miner Depos 2:113–122 **(in Chinese with English abstract)**

Zhao Y, Li D, Jingyi H, Yu J (2008a) Mineralogical characteristics of anatase, rutile and ilmenite in the Yangtizishan-Moshishan titanium ore deposit, Inner Mongolia. Miner Depos 4:466–473 **(in Chinese with English abstract)**

Zhao Y, Li D, Wu L, Ma R, Chen W, Wang P, Gao X (2008b) Two types of anatase ore shoots of different origins in the Yangtizishan-Moshishan titanium mining area, Zhenglan Prefecture, Inner Mongolia. Miner Depos 4:459–465 **(in Chinese with English abstract)**

Zhao Y, Li D, Chen W, Feng C, Sun W (2012) Moshishan metamorphic sedimentary anatase deposits: discovery, exploration and study of a new genetic type of large titanium deposit. Acta Geol Sin 86(9):1350–1365 **(in Chinese with English abstract)**

Zhou M-F, Malpas J, Song X-Y, Robinson PT, Sun M, Kennedy AK, Lesher CM, Keays RR (2002) A temporal link between the Emeishan large igneous province (SW China) and the end-Guadalupian mass extinction. Earth Planet Sci Lett 196(3–4):113–122

Zhou L, Zhang Z, Li Y, You F, Wu C, Zheng C (2013) Geological and geochemical characteristics in the paleo-weathering crust sedimentary type REE deposits, western Guizhou, China. J Asian Earth Sci 73:184–198